

## Engineering an easy-plane anisotropy in an epitaxial europium iron garnet (110) film

Yixuan Song (宋羿萱)<sup>✉</sup>, Allison C. Kaczmarek, Geoffrey S. D. Beach,<sup>\*</sup> and Caroline A. Ross<sup>†</sup>

*Department of Materials Science and Engineering, Massachusetts Institute of Technology, Cambridge, Massachusetts 02139, USA*



(Received 11 April 2023; accepted 27 July 2023; published 21 August 2023)

We demonstrate a thin film ferrimagnet, 48-nm-thick (110)-oriented europium iron garnet, in which the easy plane is perpendicular to the film plane and the hard axis lies in the film plane. We describe the individual contributions to the magnetic anisotropy and the tuning parameters that enable the easy-plane anisotropy landscape to be engineered. The anisotropy landscape is characterized using spin-Hall magnetoresistance measurements. The cubic magnetocrystalline anisotropy, often neglected for iron garnets, is shown to influence the magnetization reversal within the easy plane.

DOI: [10.1103/PhysRevMaterials.7.084407](https://doi.org/10.1103/PhysRevMaterials.7.084407)

### I. INTRODUCTION

Rare-earth iron garnets (REIG, or  $RE_3Fe_5O_{12}$ ) are cubic-structured ferrimagnetic oxides. REIGs exhibit tunable magnetic anisotropies, room temperature saturation moments up to 140 kA/m, a range of magnetization and angular momentum compensation temperatures [1–4], a low to moderate damping [5], and electrically insulating behavior. Strain-engineering of epitaxial REIG films has led to perpendicular magnetic anisotropy (PMA) in TmIG [6,7] and other REIGs as well as in Bi-substituted yttrium iron garnet (BiYIG) [8]. Films with PMA provide a convenient geometry for the observation of spin-orbit torque (SOT) switching, measurement of interfacial Dzyaloshinskii–Moriya interaction (iDMI) [9], current-driven skyrmion motion in Pt/TmIG [10] and high speed domain wall motion in Pt/BiYIG [11]. Thin film REIGs offer a range of potential applications including domain-wall memory devices [12,13], magnonic devices [14,15], and broadband microwave oscillators [16].

While magnetic films have been grown with a wide range of uniaxial anisotropies, obtaining more complex anisotropy landscapes such as biaxial and tilted easy-plane anisotropy remains an underexplored area. It was recently predicted that an easy-plane anisotropy  $90^\circ$  tilted from the film plane is critical for the specific spin-current injection geometry to experimentally demonstrate novel phenomena of spin superfluidity [17] and terahertz signal generation [18,19], both of which rely on coherent magnetization rotation within the easy plane. These applications highlight the importance of generating such anisotropy landscapes and characterizing their magnetization reversal processes.

Recent work has demonstrated tilted easy planes in anti-ferromagnetic (AFM) films. Hematite films were grown with an easy plane tilted at  $58^\circ$  with respect to the substrate plane [20] and  $Mn_3Sn$  with a  $90^\circ$  tilt angle [21]. This was accomplished by growth of these uniaxial materials on a substrate with a selected orientation in order to align the c axis in

a specific direction. Growth on low-symmetry substrate surfaces can also be used to control the magnetic anisotropy of thin films of cubic materials. Ferrimagnetic REIG films with (110) orientation were grown by liquid phase epitaxy (LPE) nearly 50 years ago, motivated by applications in magnetic bubble memory [22–25], and showed enhanced domain wall motion along the in-plane easy axis [26,27]. However, the engineering and magnetization reversal process of REIG films with a  $90^\circ$  tilted easy-plane anisotropy has not been previously explored.

Here, we select thin film  $Eu_3Fe_5O_{12}$  (EuIG) epitaxially grown on  $Gd_3Ga_5O_{12}$  (GGG) (110) substrates by pulsed laser deposition (PLD). The  $C_{2v}$  symmetry of this film orientation allows for different energies for magnetization along the in-plane [001] and  $[1\bar{1}0]$  directions. Then, we take advantage of the magnetoelastic anisotropy along with other anisotropy contributions to match the energy of the out-of-plane [110] direction to that of the in-plane easy axis  $[1\bar{1}0]$ . As a result, we successfully engineered an easy-plane anisotropy landscape in which the in-plane [001] direction, the hard axis, is normal to the easy plane. We obtain  $K_h \gg K_e$ , where  $K_e$  is the anisotropy within the easy-plane and  $K_h$  the hard-axis anisotropy. We further show that when  $K_e$  is of the same order as the small magnetocrystalline anisotropy  $K_1$ , then the magnetocrystalline anisotropy qualitatively modifies the magnetization reversal process.

### II. RESULTS AND DISCUSSION

#### A. Easy-plane anisotropy landscape definition

The easy-plane anisotropy landscape is defined in Eq. (1), where the total anisotropy energy is  $E_A$ .  $K_e$  defines the (ideally small) anisotropy energy within the easy plane and  $K_h$  defines the hard-axis anisotropy energy normal to the easy plane.  $\hat{n}_e$  and  $\hat{n}_h$  are unit vectors of the easy and hard principal axes, respectively.  $\mathbf{m}$  is the unit vector of the net magnetization. The last term in Eq. (1) is a cubic symmetry term arising from the crystal symmetry in the REIG. The desired anisotropy landscape of an easy plane perpendicular to the film plane is achieved under the condition of  $K_h \gg K_e$  and  $\hat{n}_h$  lying within

<sup>\*</sup>gbeach@mit.edu

<sup>†</sup>caross@mit.edu

TABLE I. Summary of possible anisotropy landscapes, for a given range of  $E_1$  and  $E_2$  values, which can be directly obtained from the material parameters.  $E_{\hat{n}_e}$ ,  $E_{\hat{n}_i}$ , and  $E_{\hat{n}_h}$  are energies along  $\hat{n}_e$ ,  $\hat{n}_i$ , and  $\hat{n}_h$ , respectively.

Scenario	$\hat{n}_e$	$\hat{n}_h$	$K_e$	$K_h$	$E_{\hat{n}_i} - E_{\hat{n}_e}$	$E_{\hat{n}_h} - E_{\hat{n}_i}$
$E_2 < -E_1 < -K_1/4$	$[\bar{1}10]$	$[001]$	$-(E_1 + E_2)$	$E_1$	$K_e$	$K_h - K_1/4$
$-E_1 < E_2 < -K_1/4$	$[110]$	$[001]$	$E_1 + E_2$	$-E_2$	$K_e$	$K_h - K_1/4$
$-K_1/4 < -E_1 < E_2$	$[001]$	$[\bar{1}10]$	$-E_1$	$E_1 + E_2$	$K_e + K_1/4$	$K_h$
$-E_1 < -K_1/4 < E_2$	$[110]$	$[\bar{1}10]$	$E_1$	$E_2$	$K_e - K_1/4$	$K_h + K_1/4$
$-K_1/4 < E_2 < -E_1$	$[001]$	$[110]$	$E_2$	$-(E_1 + E_2)$	$K_e + K_1/4$	$K_h$
$E_2 < -K_1/4 < -E_1$	$[\bar{1}10]$	$[110]$	$-E_2$	$-E_1$	$K_e - K_1/4$	$K_h + K_1/4$

the film plane.

$$E_A = -K_e(\mathbf{m} \cdot \hat{n}_e)^2 + K_h(\mathbf{m} \cdot \hat{n}_h)^2 + K_{\text{cubic}}(\mathbf{m}). \quad (1)$$

To understand the tuning parameters for  $K_e$  and  $K_h$ , and to define  $\hat{n}_e$  and  $\hat{n}_h$  in crystal orientations shown in Table I, we derive an expression for  $E_A$  by summing over the individual contributions for the general case of a REIG. The contributions to anisotropy energy  $E_A$  in an epitaxial single-crystal thin film include magnetocrystalline anisotropy energy ( $E_{\text{mc}}$ ), magnetostatic anisotropy energy ( $E_{\text{ms}}$ ), magnetoelastic anisotropy energy ( $E_{\text{me}}$ ), growth-induced anisotropy energy ( $E_{\text{GIA}}$ ) [28], and surface/interface anisotropy energy ( $E_{\text{surface}}$ ) [29]. The energy terms  $E_{\text{mc}}$ ,  $E_{\text{me}}$ , and  $E_{\text{GIA}}$  are described in terms of direction cosines of the magnetization with respect to the cubic crystallographic axes [30]. In order to obtain the easy-plane anisotropy defined in Eq. (1), we consider the case of an epitaxial (110)-oriented cubic crystal thin film, which has three inequivalent principal axes along  $[110]$ ,  $[\bar{1}10]$ , and  $[001]$ . The coordinate system is redefined with  $\vec{a}_1 = [\bar{1}10]$ ,  $\vec{a}_2 = [001]$ ,  $\vec{a}_3 = [110]$  as shown in Fig. 1(a). The individual contributions to the anisotropy landscape are expressed in terms of  $\theta$  and  $\phi$  in Eqs. (2)–(5) after a coordinate transformation, where  $\theta$  is the angle that the magnetization makes with the film normal  $[110]$ , and  $\phi$  is the in-plane angle, which is set to zero along the  $[\bar{1}10]$  direction.  $M_s$  is the saturation magnetization,  $B_1$  and  $B_2$  are the magnetoelastic coefficients,  $A$  and  $B$  are the growth-induced anisotropy coefficients [28], and  $K_{\text{A,surface}}$  and  $K_{\text{B,surface}}$  parametrize surface/interface anisotropy.  $B_1$  and  $B_2$  are given by  $B_1 = -\frac{3}{2}\lambda_{100}(c_{11} - c_{12})$  and  $B_2 = -3\lambda_{111}c_{44}$ , where  $c_{11}$ ,  $c_{44}$ , and  $c_{12}$  are the elastic constants,  $\lambda_{100}$  and  $\lambda_{111}$  are the magnetostriction coefficients,

and  $\epsilon$  is the coherent strain from lattice mismatch between film and substrate, given by  $\epsilon = 1 - \frac{a_{\text{film}}}{a_{\text{sub}}}$ , where  $a_{\text{sub}}$  and  $a_{\text{film}}$  are the lattice parameters for substrate and film, respectively. Constants independent of  $\theta$  and  $\phi$  are omitted from Eqs. (2)–(5) since they do not affect the equilibrium magnetization direction.

$$E_{\text{mc}}(\theta, \phi) = K_1 \left( \frac{\cos^4 \theta}{4} - \frac{\cos^2 \theta \sin^2 \theta \cos^2 \phi}{2} + \frac{\cos^4 \phi \sin^4 \theta}{4} + \cos^2 \theta \sin^2 \theta \sin^2 \phi + \cos^2 \phi \sin^2 \phi \sin^4 \theta \right) \quad (2)$$

$$E_{\text{ms}}(\theta) = -\mu_0 \frac{M_s^2}{2} \sin^2 \theta \quad (3)$$

$$E_{\text{me}}(\theta, \phi) = \epsilon \left\{ \left[ \left( \frac{3}{2}B_1 - \frac{3}{4}B_2 \right) + \left( -\frac{3}{2}B_1 - \frac{3}{4}B_2 \right) \cos^2 \phi \right] \sin^2 \theta \right\} \quad (4)$$

$$E_{\text{GIA}}(\theta, \phi) = \left[ -\left( \frac{A}{2} + \frac{B}{4} \right) + \left( \frac{A}{2} - \frac{B}{4} \right) \cos^2 \phi \right] \sin^2 \theta \quad (5)$$

$$E_{\text{surface}}(\theta, \phi) = (K_{\text{A,surface}} + K_{\text{B,surface}} \cos^2 \phi) \sin^2 \theta \quad (6)$$

$E_A$  can then be rewritten in terms of  $\theta$  and  $\phi$  as  $E_A(\theta, \phi) = E_{\text{mc}}(\theta, \phi) + (E_1 + E_2 \cos^2 \phi) \sin^2 \theta$ , where  $E_{\text{mc}}$  comprises

TABLE II. Materials parameters of EuIG. \*Example values are given for  $A$  and  $B$  to indicate a typical order of magnitude in mixed rare-earth garnets.

Materials parameters		Literature	Ref.	Experiment
Magnetocrystalline anisotropy	$K_1$	$-3.8 \text{ kJ/m}^3$	[32]	$-3.7 \pm 0.3 \text{ kJ/m}^3$
Saturation magnetization	$M_s$	$93 \text{ kA/m}$	[30]	$80 \pm 7 \text{ kA/m}$
Magnetostriction coefficients	$\lambda_{100}$	$21 \times 10^{-6}$	[33]	
	$\lambda_{111}$	$1.8 \times 10^{-6}$	[33]	
Elastic moduli	$c_{11}$	$251 \text{ GPa}$	[34]	
	$c_{12}$	$107 \text{ GPa}$	[34]	
	$c_{44}$	$76.2 \text{ GPa}$	[34]	
Growth induced anisotropy constants	A*	$-2 \text{ kJ/m}^3$		
	B*	$-5 \text{ kJ/m}^3$		

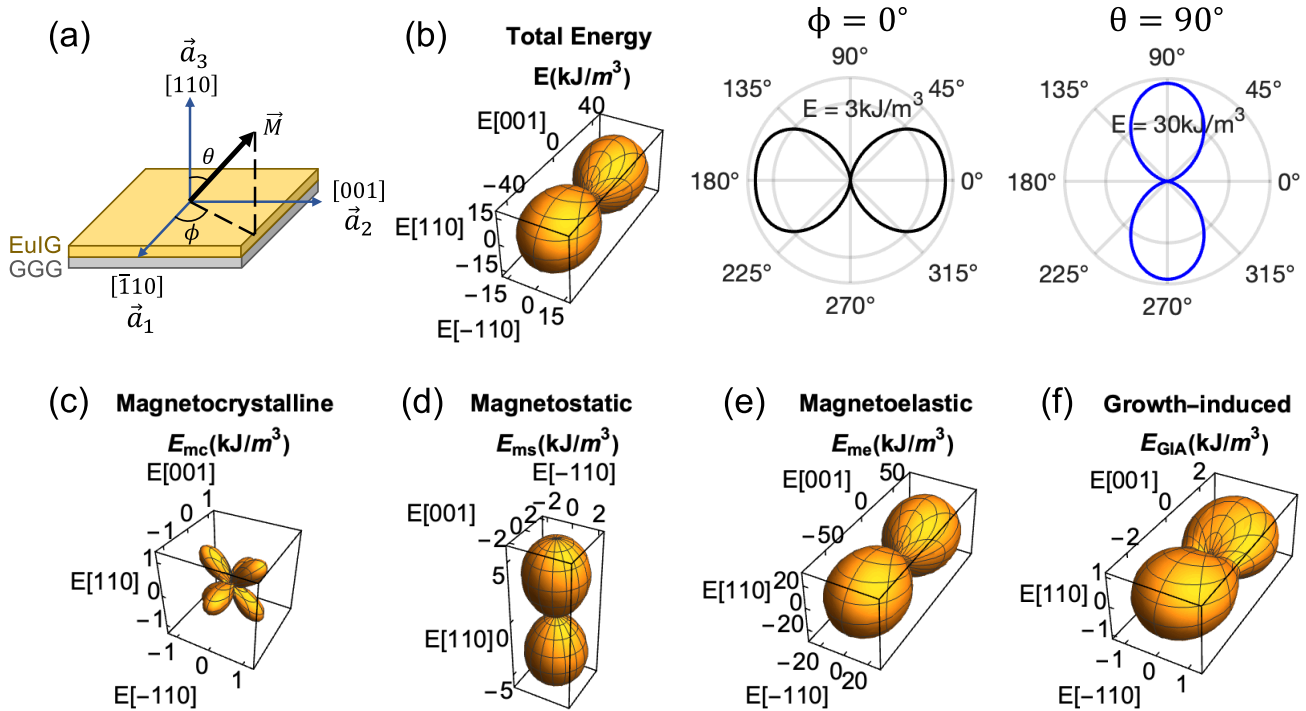


FIG. 1. (a) Definition of coordinate axes. (b) From left to right, total anisotropy energy landscape (first panel) and cross sections for  $\phi = 0^\circ$  (second panel) and  $\theta = 90^\circ$  (third panel). (c)–(f) Anisotropy landscape broken down into its individual contributions. In the polar plots, distance from plot surface to origin indicates the anisotropy energy. The individual contributions in (c)–(f) are obtained by evaluating Eqs. (2)–(5) with the anisotropy constants in Table II. In order to avoid negative values, each plot has been offset by its minimum value [e.g.,  $E_{mc}(\theta, \phi)$  plotted =  $E_{mc}(\theta, \phi)$  calculated from Eq. (2) +  $\min_{\theta, \phi}(E_{mc}(\theta, \phi))$ ]. The first panel in (b) is then obtained by the sum of the individual contributions and similarly offset by its minimum value.

the cubic symmetric component ( $K_{\text{cubic}}$ ) in Eq. (1),  $E_1 = -\frac{A}{2} - \frac{B}{4} + \frac{3B_1\epsilon}{2} - \frac{3B_2\epsilon}{4} - \frac{\mu_0 M_s^2}{2} + K_{A,\text{surface}}$  and  $E_2 = \frac{A}{2} - \frac{B}{4} - \frac{3B_1\epsilon}{2} - \frac{3B_2\epsilon}{4} + K_{B,\text{surface}}$ . With a range of material parameters contributing to  $E_1$  and  $E_2$ , several different anisotropy landscapes can be achieved in a (110) REIG film. The possible types of anisotropy landscapes, the corresponding crystallographic directions for  $\hat{n}_e$  and  $\hat{n}_h$ , and the anisotropy landscape parameters  $K_e$  and  $K_h$  in terms of  $E_1$  and  $E_2$  are summarised in Table I. (The detailed derivation for quantities in Table I is presented in Appendix A.) With  $\hat{n}_i$  defined as the intermediate anisotropy axis given by  $\hat{n}_i = \hat{n}_e \times \hat{n}_h$ , the last two columns give the absolute energy difference between  $\hat{n}_e$  and  $\hat{n}_i$  and between  $\hat{n}_e$  and  $\hat{n}_h$ , respectively, with crystalline anisotropy  $E_{mc}$  included. To facilitate rotation of the magnetization in the easy plane, it is desirable to minimize the energy difference between  $\hat{n}_e$  and  $\hat{n}_i$ . The scenarios in the first four rows give us the desirable anisotropy landscape defined in Eq. (1), i.e., the easy plane perpendicular to the film plane and the hard axis in the film plane. The last two rows have the hard axis perpendicular to the film.

### B. Case study of EuIG/GGG(110)

In this section we present a theoretical description of the anisotropy landscapes for a EuIG/GGG(110) thin film. Based on the bulk properties of all the rare-earth iron

garnets, EuIG was selected based on its relatively large (for REIGs) and dissimilar magnetoelastic coefficients. We analyzed the anisotropy landscape in EuIG/GGG(110) using the relevant material parameter values from literature summarized in Table II, which are compared with the experimentally determined values from the present paper, discussed in Sec. II C. This analysis does not consider the effects of off-stoichiometry [31] and surface/interface anisotropy [29] because their effects on the materials properties are not fully characterized.

The net anisotropy and the individual anisotropy contributions of EuIG/GGG(110) are evaluated using Eqs. (2)–(5) with the parameters in Table II and plotted in Figs. 1(b)–1(f). The panels in Fig. 1(b) from left to right show the 3D polar plot for the total anisotropy landscape, the cross section of the anisotropy landscape along  $\phi = 0^\circ$  and the cross section along  $\theta = 90^\circ$ , respectively. From the  $\phi = 0^\circ$  cross section, which shows the anisotropy landscape within the easy plane, we note that the twofold symmetry is still preserved. However, the energy no longer simply follows a  $\cos^2 \theta$  dependence because of the additional  $E_{mc}$  contribution, which is comparable in magnitude to the anisotropy within the easy plane (between axes  $[\bar{1}10]$  and  $[110]$ ). The implication of this additional contribution is discussed in Sec. II C. The cross section along  $\theta = 90^\circ$  [third panel in Fig. 1(b)] shows the anisotropy landscape normal to the easy plane (within the film plane), where we note a significant energy difference between axes  $[\bar{1}10]$

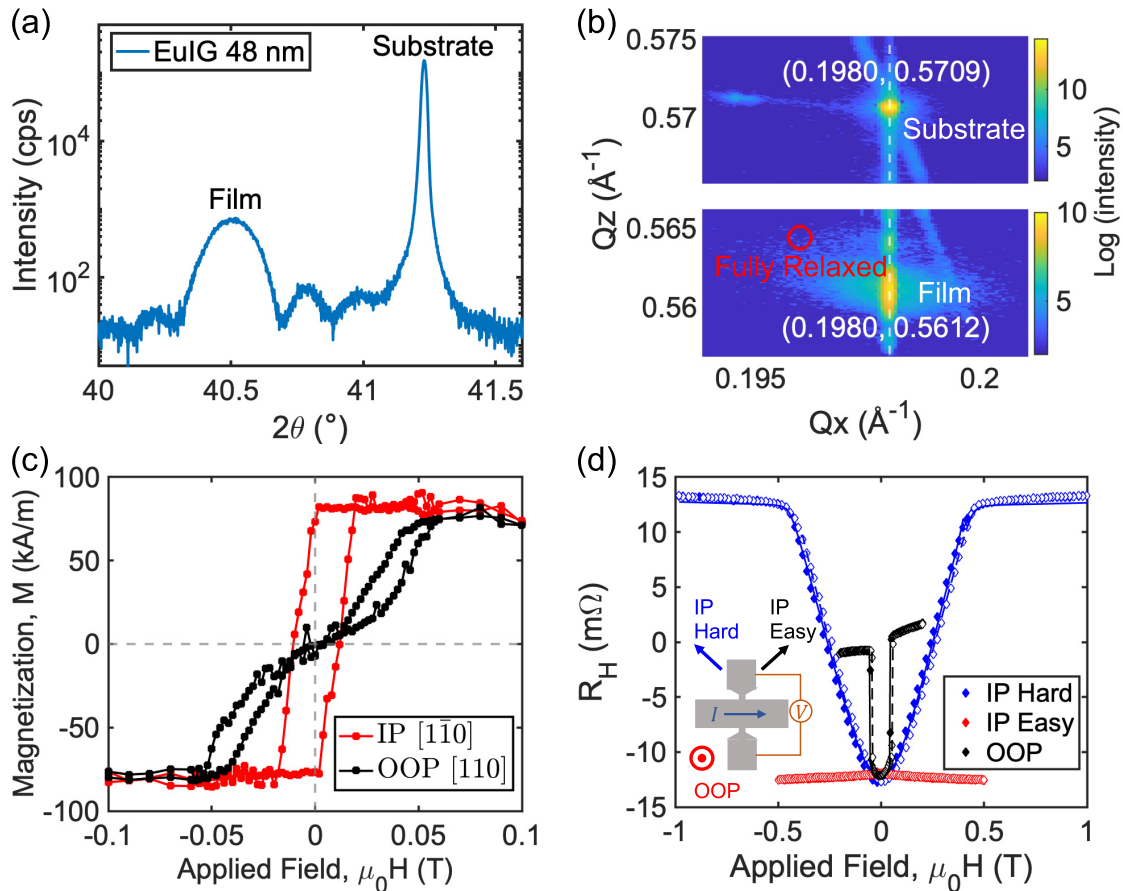


FIG. 2. (a) HRXRD measurement around the (440) reflection of the EuIG/GGG(110) film. (b) Reciprocal space map of the (642) reflection, showing fully strained film on substrate. (c) VSM hysteresis loops with field along the in-plane (IP)  $[\bar{1}10]$  direction and out-of-plane (OOP)  $[110]$  direction. (d) SMR measurements with the field applied along IP  $[\bar{1}10]$ , IP  $[001]$ , and OOP  $[110]$ . Open symbols are experimental data, and lines represent fits from the model (solid: negative to positive field sweep, dashed: positive to negative field sweep). Measurement geometry is shown in the inset.

and  $[001]$ . The anisotropy landscape is therefore dominated by terms with  $\sin^2 \phi$  dependence.

Although the GIA terms  $A$  and  $B$  are not expected to be present in the EuIG film, the inclusion of the GIA term maintains the generality of the expression. The nominally stoichiometric EuIG should have no growth-induced anisotropy; however, deviations from the ideal composition could produce vacancy ordering on the iron sites or cation antisite defects that can cause GIA [7]. Typical values of  $A$  and  $B$  for mixed garnets are given in Table II for comparison. The quantities related to  $K_{\text{surface}}$  for EuIG are not available in literature and are not included here. We will present a characterization of the surface anisotropy of EuIG films elsewhere. Comparison between the first panel in Figs. 1(b) and 1(e) shows that for a EuIG film on (110) GGG, the anisotropy landscape is dominated by the magnetoelastic contribution.

### C. Characterization of the anisotropy landscape in EuIG/GGG(110)

A 48-nm-thick EuIG film was grown on a (110)-orientated GGG substrate using pulsed laser deposition (PLD) under

the conditions described in Sec IV. High-resolution x-ray diffractometry (HRXRD) of the (440) reflection is shown in Fig. 2(a). The film peak position and Laue fringes were fitted to extract the  $d_{440}$  plane spacing of  $1.259/(4\sqrt{2}) \pm 0.001$  nm and the EuIG film thickness of  $48.5 \pm 0.1$  nm. The  $d_{440}$  value from HRXRD agrees well with the (440) plane spacing based on a fully strained film with a Poisson ratio of 0.29 [35]. A detailed calculation for the expected  $d_{440}$  in fully strained EuIG/GGG(110) can be found in Appendix B. The reciprocal space map (RSM) for the (642) reflection in Fig. 2(b) shows a fully strained film with in-plane lattice match to the substrate (the peaks have the same  $Q_x$  value within instrument resolution). The red circle indicates the expected peak position for a fully relaxed film. Scanning transmission electron microscopy measurements in Fig. 1(e) of Ref. [6] and Fig. 1(c) of Ref. [9] indicate interface coherency and structural uniformity in PLD-grown REIG films with similar thickness to the EuIG film of the present study, confirming that REIG films can retain their lattice mismatch strain up to thicknesses of tens of nm.

Vibrating sample magnetometry (VSM) in Fig. 2(c) yields a saturation magnetization of  $80 \pm 7$  kA/m, which is slightly

lower than the bulk value of 93 kA/m. The difference may indicate an iron deficiency [7] or a change of Eu oxidation state [36]. The saturation field along the [001] in-plane hard axis was too high to be determined using VSM due to the large nonlinear background of GGG at high fields. [The VSM hysteresis loops for EuIG/GGG(110) sample and GGG substrate at high fields are shown in Fig. 5 in Appendix C.] The easy axis is along the in-plane (IP)  $[\bar{1}10]$  direction, producing a square hysteresis loop, while the out-of-plane (OOP) [110] direction is an intermediate axis, which saturates at a field of  $\mu_0 H = 0.06$  T.

A spin-Hall magnetoresistance (SMR) measurement [37,38], described in Sec. IV, was performed to quantitatively determine the anisotropy fields, which characterize the easy-plane anisotropy landscape. We measured the transverse Hall resistance with fields swept along the in-plane  $[\bar{1}10]$  and [001] and the out-of-plane [110] direction, shown in Fig. 2(d), labeled as IP Easy, IP Hard, and OOP, respectively. The measurement geometry is shown in the inset of the same figure. An in-plane electrical current in Pt generates an out-of-plane spin current through the spin-Hall effect (SHE). The spin current will be partially reflected with a magnitude dependent on the magnetization direction in EuIG, which converts back to a charge current through inverse SHE leading to a change in the Pt resistance. Changes in the equilibrium magnetization direction in EuIG with applied field are therefore detected via the transverse and longitudinal resistance in Pt.

It is well established that the transverse Hall resistance ( $R_H$ ) in a REIG/Pt bilayer consists of the components in Eq. (7) [38,39] where  $R_{\text{SMR}}$  and  $R_{\text{SMR,AHE}}$  represent the manifestation of SMR and the SMR-induced anomalous Hall effect (AHE) resistance, respectively and  $R_{\text{OHE}}$  is the ordinary Hall effect resistance.  $H_3$  is the out-of-plane applied magnetic field and  $m_i$  are the components of the magnetization direction vector  $\vec{m}$ ,

$$R_H = R_{\text{SMR,AHE}} m_3 + R_{\text{SMR}} m_1 m_2 + R_{\text{OHE}} \mu_0 H_3. \quad (7)$$

Using the coordinate system defined in Fig. 1(a),  $\theta$  and  $\phi$  are the polar and azimuthal angles, respectively, of the equilibrium magnetization and  $\phi_I$  is the angle between the charge current and the  $[\bar{1}10]$  direction. The SMR expression can be re-written in terms of  $\theta$  and  $\phi$  in Eq. (8). We applied charge current at  $45^\circ$  ( $\phi_I = \pi/4$ ) to the principal in-plane anisotropy axes for ease of interpretation.

$$R_H = R_{\text{SMR,AHE}} \cos \theta + R_{\text{SMR}} \sin^2 \theta \sin 2(\phi - \phi_I) + R_{\text{OHE}} \mu_0 H_3. \quad (8)$$

From the SMR measurement along the three principal axes, we extract  $R_{\text{SMR,AHE}} = 0.42$  m $\Omega$ ,  $R_{\text{SMR}} = 12.46$  m $\Omega$ , and  $R_{\text{OHE}} = 4.47$  m $\Omega$  T $^{-1}$ , which translates to resistivity changes  $\Delta \rho_{\text{SMR}} = 5.0 \times 10^{-3}$   $\mu\Omega$  cm,  $\Delta \rho_{\text{SMR,AHE}} = 1.7 \times 10^{-4}$   $\mu\Omega$  cm, and  $\Delta \rho_{\text{OHE}} = 1.8 \times 10^{-3}$   $\mu\Omega$  cm T $^{-1}$ . From the theory of [38] and taking the value of spin Hall angle of Pt to be 0.08 and the spin-diffusion length to be 1.4 nm [40,41], the real and imaginary parts of the spin mixing conductance can be derived as  $G_r = 1.07 \times 10^{14}$   $\Omega^{-1}$  m $^{-2}$  and  $G_i = 1.39 \times 10^{12}$   $\Omega^{-1}$  m $^{-2}$ , which compare well with reported values [36].

Simulation of the magnetic reversal process was performed using a macrospin model, where the equilibrium magnetiza-

tion direction was determined by minimizing the total energy in Eq. (9) with respect to  $\theta$  and  $\phi$ .  $\theta_H$  and  $\phi_H$  are the polar and azimuthal angles for the applied field direction with respect to the coordinate system in Fig. 1(a),

$$\begin{aligned} E_{\text{tot}} &= E_A + \mu_0 \vec{M} \cdot \vec{H} \\ &= E_A + \mu_0 M_s H (\cos \phi \sin \theta \cos \phi_H \sin \theta_H \\ &\quad + \sin \phi \sin \theta \sin \phi_H \sin \theta_H + \cos \phi \cos \theta_H). \end{aligned} \quad (9)$$

We extracted the anisotropy values by performing a numerical fit of the SMR measurement results to this macrospin model. For each applied field, we determined the equilibrium magnetization direction in terms of  $\theta$  and  $\phi$  by minimizing Eq. (9) and substituted the values into Eq. (8). Figure 2(d) shows the experimental data plotted together with the fit.  $E_1$  and  $E_2$  in  $E_A$  were optimized by minimizing the mean squared error between experimental and fit SMR values.  $E_1$  and  $E_2$  are then converted to  $K_h$  and  $K_e$  through the equations in the first row of Table I. The fit gave  $K_h = 10 \pm 1$  kJ/m $^3$ ,  $K_e = 2.7 \pm 0.3$  kJ/m $^3$ , and  $K_1 = -3.7 \pm 0.3$  kJ/m $^3$ .  $K_1$ , the magnetocrystalline anisotropy coefficient, is close to the bulk value of  $-3.8$  kJ/m $^3$  in EuIG reported in literature [32,42].

The anisotropy landscape now satisfies the conditions given in Eq. (1) with  $\hat{n}_e \parallel [\bar{1}10]$ ,  $\hat{n}_i \parallel [110]$ , and  $\hat{n}_h \parallel [001]$ , i.e., the hard axis is within the film plane, and the (001) plane exhibits a small anisotropy  $K_e$ . Options to further optimize the anisotropy landscape by maximizing  $K_h$  and minimizing  $K_e$  include lowering the saturation magnetization, e.g., by substituting Fe $^{3+}$  with Al $^{3+}$ . The magnetostatic anisotropy [Eq. (3)] lowers the energy for in-plane magnetization; for our EuIG/GGG(110) energy landscape, lowering the magnetostatic anisotropy would reduce  $K_e$ . Doping with other rare-earth ions can also lower  $K_e$  through growth-induced anisotropy. However, changes in composition will also affect magnetoelastic and magnetocrystalline contributions. To maximize  $K_h$ , one could increase the magnetoelastic contribution through growth on a smaller lattice parameter substrate (though such substrates, e.g., Al-substituted GGG, are not commercially available). Additional tuning through changes in thickness (modifying the contribution of surface/interface anisotropy) and/or temperature (via the temperature dependence of  $B_1$ ,  $B_2$ ,  $M_s$ ,  $K_1$ , etc.) will be described in a separate article.

#### D. Modelling the switching behaviour within the easy-plane

For a field along the intermediate anisotropy axis [110] ( $\hat{n}_i$ ), both the VSM [Fig. 2(c) OOP [110] plot] and SMR [Fig. 2(d) OOP plot] measurements show hysteresis loops that differ from that of a hard or easy axis macrospin model. We will now show that this switching behavior within the easy plane (constructed by IP  $[\bar{1}10]$  ( $\hat{n}_e$ ) and OOP [110] ( $\hat{n}_i$ ) directions) originates from the small cubic magnetocrystalline anisotropy. Considering Eq. (1), the anisotropy landscape differs from that of a system with easy-plane anisotropy by addition of the magnetocrystalline anisotropy term  $E_{\text{mc}}$ . From the plots in Figs. 1(c)–1(e),  $E_{\text{mc}}$  appears to be small compared to the magnetoelastic  $E_{\text{me}}$  and shape anisotropy  $E_{\text{ms}}$  contributions. However, when the anisotropy  $K_e$  within the easy plane

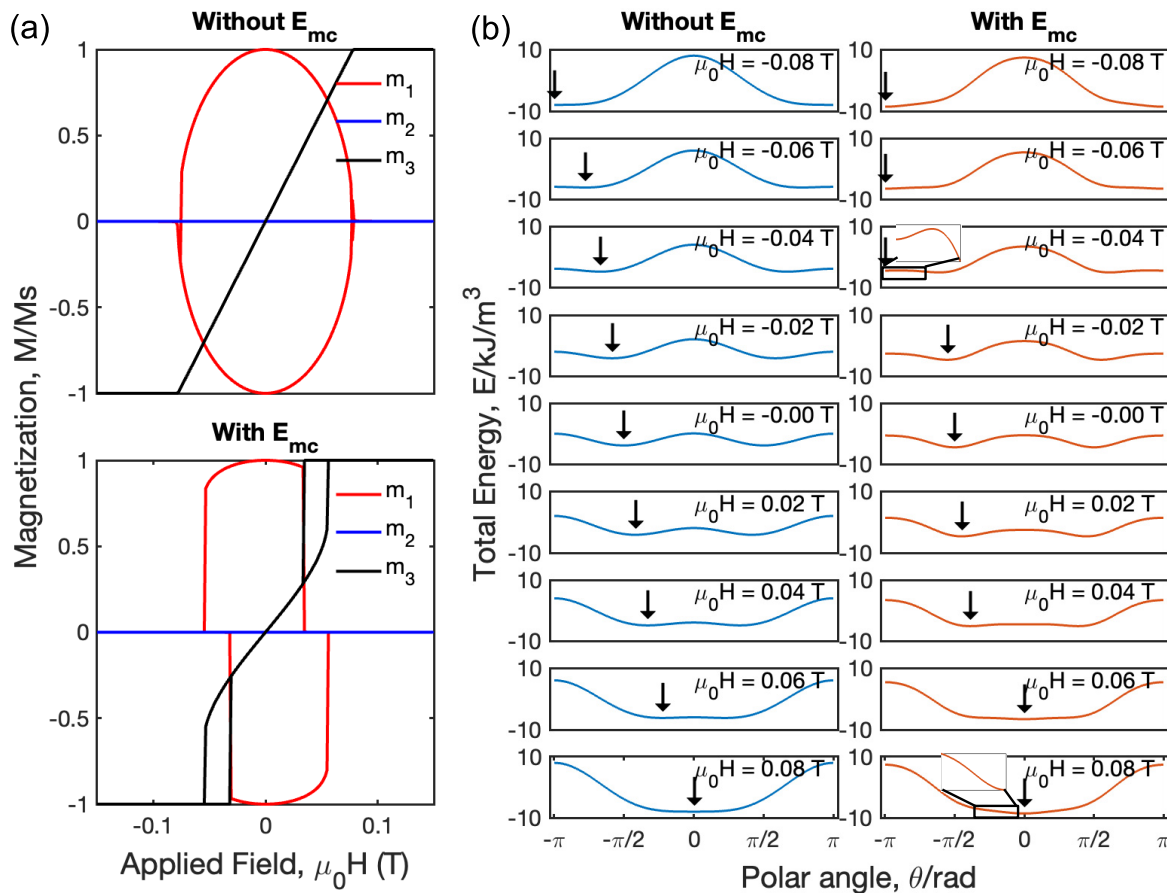


FIG. 3. (a) The simulated magnetization components vs field neglecting magnetocrystalline anisotropy (top panel) and considering magnetocrystalline anisotropy (bottom panel). Field is swept along the out-of-plane (OOP) [110] direction. (b) Total out-of-plane energy landscape evolution as a function of applied field with and without magnetocrystalline anisotropy.

has the same magnitude as  $E_{mc}$ , the effects of  $E_{mc}$  become evident in the switching behavior. This explains why the VSM data in Fig. 2(c) for an out-of-plane field (i.e., a field along the intermediate axis [110]) shows hysteretic magnetization reversal via a low remanence state. The low remanence is not a result of domain formation, rather, the equilibrium magnetization direction is in-plane at zero-field to give the observed SMR signal.

With the macrospin model described in Sec. II C, we modeled the magnetization switching behavior with field swept along  $\hat{n}_i$  (Fig. 3), where the equilibrium magnetization components are determined as a function of applied field. The switching behavior in Fig. 2(c) OOP [110] plot could not be reproduced unless the cubic anisotropy term is included. As shown in the top panel of Fig. 3(a), the  $K_e$  and  $K_h$  terms predict a hard-axis behavior for the out-of-plane component of magnetization ( $m_3$ ). However, with the addition of magnetocrystalline anisotropy, the model [bottom panel of Fig. 3(a)] qualitatively reproduced the switching behavior in the OOP [110] plot of Fig. 2(c).

Although magnetocrystalline anisotropy is usually neglected in iron garnets, the (110) EuIG/GGG provides a case where inclusion of magnetocrystalline anisotropy is essential to model the reversal behavior. This arises because the easy-

plane anisotropy is small enough that the magnetocrystalline anisotropy dominates the response of the magnetization to field cycling ( $K_1 \approx K_e$ ). The  $\theta$  cross section of the energy landscape during the switching process for an out-of-plane field sweep is shown in Fig. 3(b). Although the plots look similar with and without  $E_{mc}$ , the equilibrium position of magnetization indicated by the arrow position is different. On the left panels, without the magnetocrystalline anisotropy contribution, the magnetization undergoes a smooth transition as the external field is swept from upward to downward. On the right panel, the local perturbations caused by magnetocrystalline anisotropy [insets in Fig. 3(b)] create local minima, which lead to jumps in the magnetization direction between the third and fourth panels as well as the seventh and eighth panels.

We further modelled the SMR measurement result ( $R_H$  vs  $\mu_0 H$ ) with field applied along the three principal anisotropy axes ( $\hat{n}_i = [110]$ ,  $\hat{n}_h = [001]$  and  $\hat{n}_e = [\bar{1}10]$ ) by substituting the equilibrium magnetization directions determined with the macrospin model (described in Sec. II C) into Eq. (8). With the SMR measurement geometry shown in Fig. 4 and described in Sec. IV,  $R_H = -R_{SMR}$  and  $R_{SMR}$  when magnetization is fully saturated along  $\hat{n}_e = [\bar{1}10]$  and  $\hat{n}_h = [001]$ , respectively. Firstly,  $R_H(H = 0T) = -R_{SMR}$  for all plots in Fig. 4 unambiguously confirmed that the equilibrium magnetization

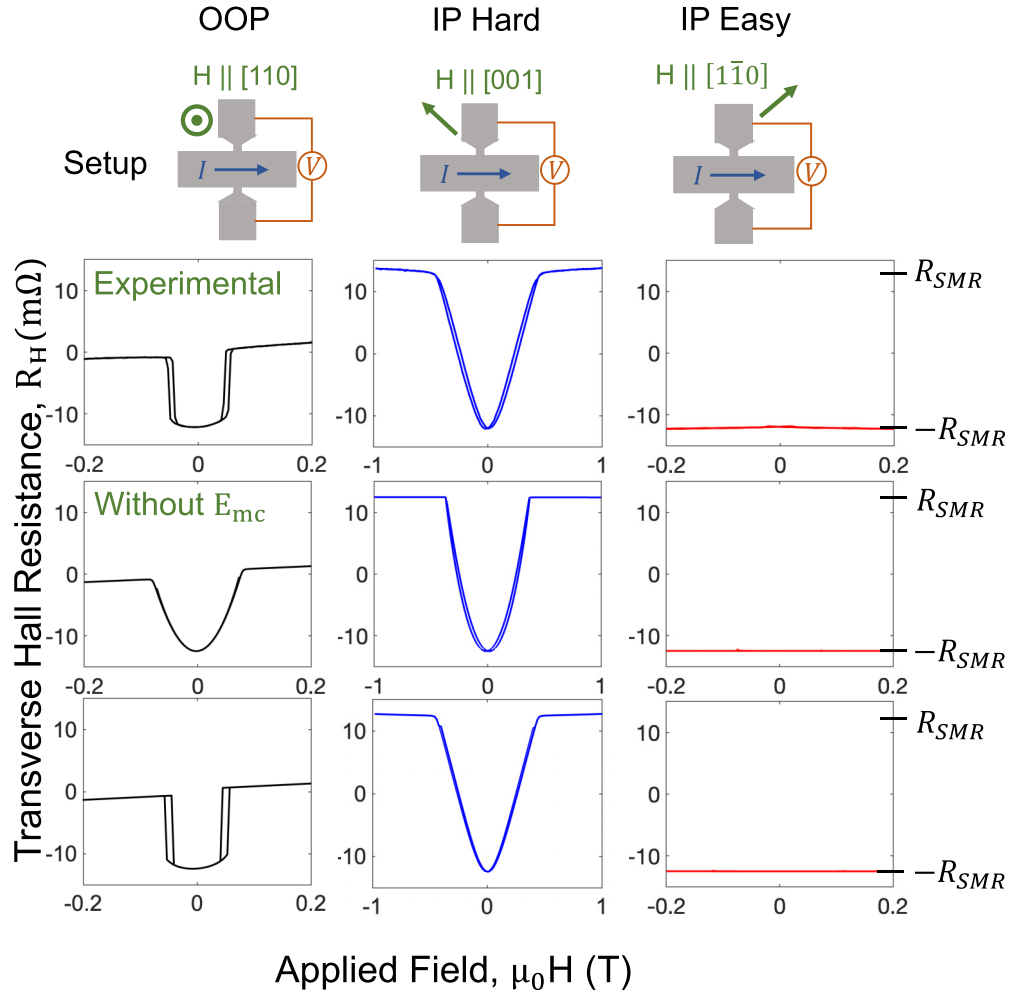


FIG. 4. Geometry of the SMR measurement and a comparison between experimental data and model prediction. The current is applied at  $45^\circ$  from the  $[001]$  and  $[\bar{1}10]$  directions. The first row of plots shows the experimental measurement along the three axes. The second (third) row shows simulations of the SMR signal for the anisotropy analysis without (with) the magnetocrystalline anisotropy included.

direction at remanence is along  $\hat{n}_e$ . Secondly, from the plots in the first column showing field applied along  $\hat{n}_i = [110]$ , we observe a similar switching behavior between experiment and model with  $E_{mc}$ . (Switching again is not captured in a model without  $E_{mc}$ .) Since the SMR measurement is sensitive to both in-plane and out-of-plane magnetization components, the resemblance between modelled plot and experimentally obtained results gives further confirmation that the magnetization reversal process is fully captured. Thirdly, in the second column where field is applied along  $\hat{n}_h = [001]$ , the presence of magnetocrystalline anisotropy has a noticeable effect on the curvature. This is another result of its perturbation of the anisotropy landscape, which affects the equilibrium magnetization direction.

Although fitting to the SMR results along both intermediate and hard axes gave a value for the magnetocrystalline anisotropy constant ( $K_1$ ), fitting to the intermediate axis data gave an underestimation of  $K_1$  because switching occurs before the energy barrier is reduced to zero. This is because switching occurs through nucleation and propagation of domains similar to the magnetization reversal of a PMA film in

an OOP field. Thermal activation across the energy barrier can also decrease the switching field. Therefore, a more reliable  $K_1$  is obtained from fitting to the curvature along the hard axis. The effect of the magnetocrystalline anisotropy on the hysteresis loops for a range of easy-plane conditions has been plotted in Fig. 6 in Appendix D.

### III. CONCLUSION

We have demonstrated an easy-plane anisotropy in a film of EuIG/GGG(110) in which the easy plane (001) is perpendicular to the plane of the sample, (110), by taking advantage of the large and dissimilar magnetoelastic coefficients of EuIG and the lattice mismatch between EuIG and GGG. The easy-plane anisotropy landscape is characterized by a hard-axis anisotropy of  $K_h = 10(1)$  kJ/m<sup>3</sup> along  $[001]$  and a easy-axis anisotropy of  $K_e = 2.7(3)$  kJ/m<sup>3</sup> along  $[\bar{1}10]$ . The cubic magnetocrystalline anisotropy becomes comparable to the easy-plane anisotropy and leads to non-negligible effects on the magnetization switching behavior, from which we extracted a magnetocrystalline anisotropy

of  $K_1 = -3.7(3) \text{ kJ/m}^3$ , similar to the bulk value. The demonstration of easy-plane anisotropy out of the film plane provides an experimental system for the study of SOT effects and magnetization dynamics, which rely on easy out-of-plane magnetization rotation. This includes but is not limited to spin-torque oscillators whose frequency is tunable from GHz to THz, the study of spin superfluidity, and anisotropic domain wall motion.

#### IV. METHODS

The EuIG thin films were grown on GGG (110) substrates (MTI Corporation) by pulsed laser deposition with a 248-nm wavelength KrF excimer laser at an energy of 350 mJ and a repetition rate of 10 Hz using 10 000 shots [7,43,44]. The target used was a commercially available EuIG target with a 99.99% elemental purity. The growth atmosphere was oxygen at 150 mTorr with a base pressure of  $5 \times 10^{-6}$  Torr. Film thickness of 48 nm was measured by fitting data from a Bruker D8 high resolution x-ray diffractometer, and the reciprocal space map was performed on the same equipment to show in-plane lattice matching of the garnet film and substrate.

Four-nanometer Pt was sputtered on EuIG(48 nm)/GGG[110] from a 1-inch Pt target using a d.c. sputter system with Ar pressure of 3 mTorr and base pressure of  $5 \times 10^{-8}$  Torr. The sputter power was 20 W with a sputter rate of 2 nm/min calibrated using garnet substrates. Hall crosses were patterned with positive photoresist AZ3312 using a Heidelberg MLA 150 direct-write lithography system and developed with AZ 300 MIF developer. Devices in Pt/EuIG were patterned by Ar ion milling. The current arm of the device was aligned to  $45^\circ$  from the in-plane principal anisotropy axes to maximize the in-plane signal. Specifically for MTI Corporation GGG(110) substrates with  $[11\bar{1}]$  edges, the  $[\bar{1}10]$  and  $[001]$  directions are  $35$  and  $-55$  degrees from the edge. Second layer Ta(6)/Au(150) contacts were patterned to enhance current density uniformity and wire-bonding repeatability via lift-off of a PMGI/AZ3312 resist bilayer to give a desirable undercut.

Spin-Hall magnetoresistance measurements were performed on a custom-built transport measurement setup at room temperature ( $\sim 22^\circ \text{ C}$ ). The current was applied through a SR830 lock-in amplifier at a frequency of 9.973 kHz and a voltage amplitude of 5 V. Device resistance was typically  $100 \Omega$ . A 10-k $\Omega$  resistor was connected in series to provide a stable current source. The transverse voltage was differentially fed back to the lock-in amplifier. Measurements were automated with a Labview program.

#### ACKNOWLEDGMENTS

The authors would like to acknowledge insightful discussions with Siying Huang and Hao Tang. We thank Prof. Luqiao Liu for sharing the ion-milling facility. The authors acknowledge support from SMART, an nCORE Center supported by SRC and NIST, and NSF Grant No. ECCS 1954606. Characterization was performed in part in MIT Materials Research Laboratory shared facilities supported by the MRSEC

Program No. DMR1419807. This work was performed in part in the MIT.nano Facilities.

#### APPENDIX A: DERIVATION FOR TABLE I IN MAIN TEXT

We start with the equation

$$E_A = E_{mc}(\theta, \phi) + (E_1 + E_2 \cos^2 \phi) \sin^2 \theta \quad (\text{A1})$$

where

$$\begin{aligned} E_{mc}(\theta, \phi) = & K_1 \left( \frac{1}{4} \cos^4 \theta - \frac{1}{2} \cos^2 \theta \sin^2 \theta \cos^2 \phi \right. \\ & + \frac{1}{4} \cos^4 \phi \sin^4 \theta + \cos^2 \theta \sin^2 \theta \sin^2 \phi \\ & \left. + \cos^2 \phi \sin^2 \phi \sin^4 \theta \right). \end{aligned} \quad (\text{A2})$$

The anisotropy energies along  $[\bar{1}10]$ ,  $[110]$ , and  $[001]$  are obtained by setting  $(\theta, \phi)$  to be  $(0, \pi/2)$ ,  $(0, 0)$ , and  $(\pi/2, \pi/2)$ , respectively. This yields  $E[\bar{1}10] = E_1 + E_2 + K_1/4$ ,  $E[110] = K_1/4$ , and  $E[001] = E_1$ . For the case in the first row of Table I:  $E_2 < -E_1 < -K_1/4$ , we obtain  $E[110] - E[\bar{1}10] = -(E_1 + E_2) > 0$  and  $E[001] - E[110] = -K_1/4 + E_1 > 0$  and therefore, the direction with lowest anisotropy energy (easy axis) is  $\hat{n}_e = [\bar{1}10]$ , the direction with intermediate anisotropy energy (intermediate axis) is  $\hat{n}_i = [110]$  and the direction with highest anisotropy energy (hard axis) is  $\hat{n}_h = [001]$ . From the definitions in Eq. (1),  $K_e$  and  $K_h$  are the energy difference between  $\hat{n}_i = [110]$  and  $\hat{n}_e = [\bar{1}10]$ , and between  $\hat{n}_h = [110]$  and  $\hat{n}_i = [\bar{1}10]$ , respectively, without the magnetocrystalline anisotropy contribution. Therefore,  $K_e = -(E_1 + E_2)$  and  $K_h = E_1$ . The last two columns are the energy difference between  $\hat{n}_i = [110]$  and  $\hat{n}_e = [\bar{1}10]$ , and between  $\hat{n}_h = [110]$  and  $\hat{n}_i = [\bar{1}10]$  with magnetocrystalline anisotropy terms included. Therefore,  $E_{\hat{n}_i} - E_{\hat{n}_e} = E[110] - E[\bar{1}10] = K_e$ , and  $E_{\hat{n}_h} - E_{\hat{n}_i} = E[001] - E[110] = K_h - K_1/4$ .

#### APPENDIX B: CALCULATION FOR EXPECTED (440) PLANE SPACING IN FULLY STRAINED FILM

Assuming coherent strain within film plane from lattice mismatch, the strain tensor is written as (in the coordinate system defined in main text)

$$\epsilon = \epsilon \begin{pmatrix} 1 & 0 & 0 \\ 0 & 1 & 0 \\ 0 & 0 & -\frac{2v}{1-v} \end{pmatrix}. \quad (\text{B1})$$

With lattice mismatch strain  $\epsilon = \frac{a_{\text{GGG}} - a_{\text{EuIG}}}{a_{\text{EuIG}}} = \frac{1.2376 - 1.2498}{1.2498} = -9.8 \times 10^{-3}$ , the (110) plane spacing in epitaxial EuIG on GGG(110) is  $a_{\text{EuIG}}/\sqrt{2} \times (1 - \frac{2v}{1-v}\epsilon) = 1.2598/\sqrt{2} \text{ nm}$ . The expected (440) plane spacing is therefore  $1.2598/4\sqrt{2} \text{ nm}$ . This calculated plane spacing agrees within the error bar from fitting to HRXRD (440) reflection. Dislocations are generally absent in such epitaxial thin films, confirmed by previous STEM measurements in Fig. 1(e) of [6] and Fig. 1(c) of [9]. Therefore, the elastic assumption can be considered valid.

## APPENDIX C: VSM MEASUREMENT OF SUBSTRATE AND EuIG AT HIGH FIELDS

We measured the net magnetic moment of the EuIG film and the GGG substrate at a large field range (- 1 T and 1 T) in Fig. 5(a). The magnetic moment is dominated by the paramagnetic signal from the GGG substrate because the thickness of the substrate (0.5 mm) is much larger than the thickness of the film (48 nm). The magnetic moment from GGG itself is shown in Fig. 5(c). After a linear background subtraction (red line), the paramagnetic signal from GGG becomes non-linear at a field below 0.2 T as shown in Fig. 5(d). We therefore determined the net magnetization from EuIG by subtracting the linear background obtained from fitting to data points below 0.1 T in Fig. 5(a). The hysteresis loop after background subtraction is shown in Fig. 5(b).

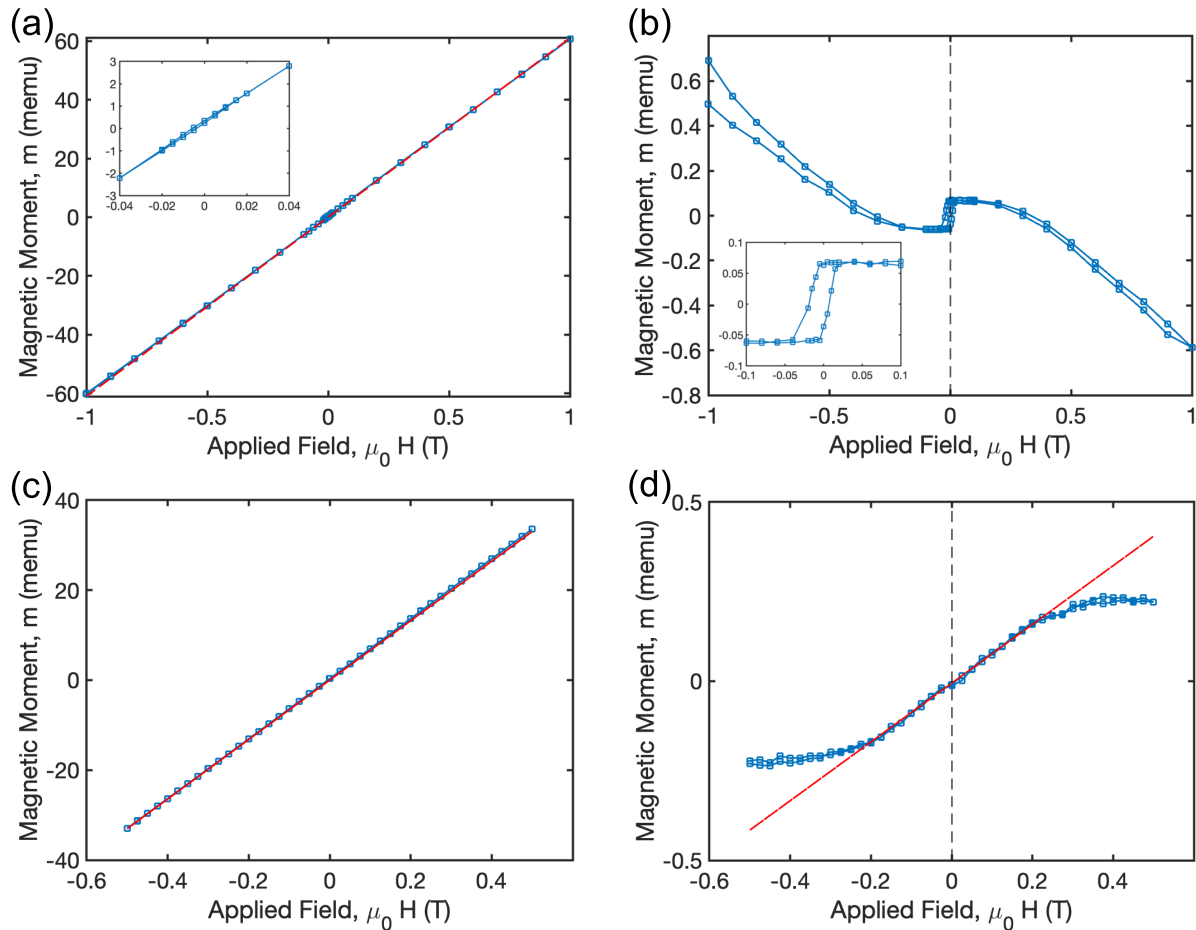


FIG. 5. (a),(b) VSM hysteresis loop for EuIG(48nm)/GGG(110) along in-plane  $[\bar{1}10]$  (a) before and (b) after linear background subtraction. A magnified plot is shown in the the insets. Red line in (a) shows the fitted linear background subtracted to obtain (b). (c),(d) VSM hysteresis loop for GGG substrate (c) before and (d) after linear background subtraction. Red line in (c) shows the fitted linear background subtracted to obtain (d). Red line in (d) shows the linear paramagnetic behavior of GGG below  $\sim 0.2$  T, above which the nonlinearity increases.

## APPENDIX D: EFFECT OF MAGNETOCRYSTALLINE ANISOTROPY ON THE PREDICTED SMR SIGNATURE

Fig. 6 shows the expected SMR signature in the REIG/GGG (110) system. We explored the effect of magnetocrystalline anisotropy by scanning across the parameter space of  $K_e$  from 5 to  $-3 \text{ kJ/m}^3$  and  $K_1$  from  $-0.6$  to  $-1.4 \text{ kJ/m}^3$ . Magnetocrystalline anisotropy clearly had an effect on creating hysteresis along the intermediate anisotropy axis in the third and fourth row where the  $K_1$  becomes comparable with  $K_e$ .

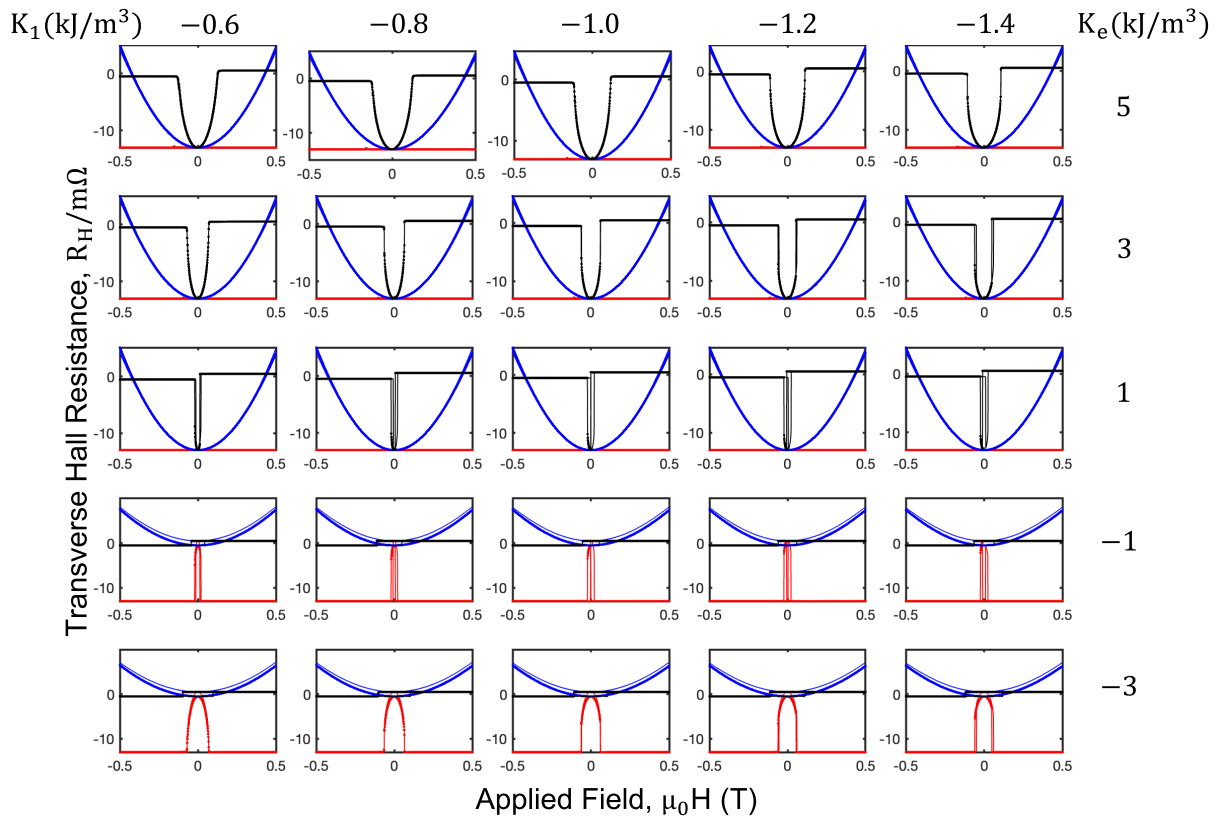


FIG. 6. The effect of magnetocrystalline anisotropy  $E_{mc}$  parameterized by  $K_1$  on the switching behavior and the corresponding SMR signature for a combination of anisotropy landscape parameters. Color scheme follows Fig. 4.  $K_e < 0$  suggests  $[110]$  axis is lowest in energy, while  $K_e > 0$  suggests  $[\bar{1}10]$  is lowest in energy. The simulation is performed with  $K_h = 21 \text{ kJ/m}^3$ .  $E_{mc}$  causes qualitative changes in the switching behavior in the third and fourth row, where  $K_1 \sim K_e$ .

- 
- [1] C. D. Brandle and S. L. Blank, Magnetic moments for mixed substituted rare earth iron garnets, *IEEE Trans. Magn.* **12**, 14 (1976).
- [2] G. F. Dionne, Molecular field coefficients of substituted yttrium iron garnets, *J. Appl. Phys.* **41**, 4874 (1970).
- [3] G. F. Dionne, *Magnetic Oxides* (Springer US, New York, 2009).
- [4] E. R. Rosenberg, K. Litzius, J. M. Shaw, G. A. Riley, G. S. D. Beach, H. T. Nembach, and C. A. Ross, Magnetic properties and growth-induced anisotropy in yttrium thulium iron garnet thin films, *Adv. Electron. Mater.* **7**, 2100452 (2021).
- [5] G. P. Vella-Coleiro, D. Smith, and L. V. Uitert, Damping of domain wall motion in rare-earth iron garnets, *Appl. Phys. Lett.* **21**, 36 (1972).
- [6] A. Quindeau, C. O. Avci, W. Liu, C. Sun, M. Mann, A. S. Tang, M. C. Onbasli, D. Bono, P. M. Voyles, Y. Xu *et al.*,  $\text{TM}_3\text{Fe}_5\text{O}_{12}/\text{Pt}$  heterostructures with perpendicular magnetic anisotropy for spintronic applications, *Adv. Electron. Mater.* **3**, 1600376 (2017).
- [7] E. R. Rosenberg, L. Beran, C. O. Avci, C. Zeledon, B. Song, C. Gonzalez-Fuentes, J. Mendil, P. Gambardella, M. Veis, C. Garcia, G. S. D. Beach, and C. A. Ross, Magnetism and spin transport in rare-earth-rich epitaxial terbium and europium iron garnet films, *Phys. Rev. Mater.*, **2**, 094405 (2018).
- [8] L. Soumah, N. Beaulieu, L. Qassym, C. Carrétéro, E. Jacquet, R. Lebourgeois, J. B. Youssef, P. Bortolotti, V. Cros, and A. Anane, Ultra-low damping insulating magnetic thin films get perpendicular, *Nat. Commun.* **9**, 3355 (2018).
- [9] L. Caretta, E. Rosenberg, F. Büttner, T. Fakhrol, P. Gargiani, M. Valvidares, Z. Chen, P. Reddy, D. A. Muller, C. A. Ross, and G. S. D. Beach, Interfacial Dzyaloshinskii-Moriya interaction arising from rare-earth orbital magnetism in insulating magnetic oxides, *Nat. Commun.* **11**, 1090 (2020).

- [10] S. Vélez, S. Ruiz-Gómez, J. Schaab, E. Gradauskaite, M. S. Wörnle, P. Welter, B. J. Jacot, C. L. Degen, M. Trassin, M. Fiebig, and P. Gambardella, Current-driven dynamics and ratchet effect of skyrmion bubbles in a ferrimagnetic insulator, *Nat. Nanotechnol.* **17**, 834 (2022).
- [11] L. Caretta, S.-H. Oh, T. Fakhru, D.-K. Lee, B. H. Lee, S. K. Kim, C. A. Ross, K.-J. Lee, and G. S. D. Beach, Relativistic kinematics of a magnetic soliton, *Science* **370**, 1438 (2020).
- [12] S. S. P. Parkin, M. Hayashi, and L. Thomas, Magnetic domain-wall racetrack memory, *Science* **320**, 190 (2008).
- [13] S. Parkin and S.-H. Yang, Memory on the racetrack, *Nat. Nanotechnol.* **10**, 195 (2015).
- [14] Y. Kajiwara, K. Harii, S. Takahashi, J. Ohe, K. Uchida, M. Mizuguchi, H. Umezawa, H. Kawai, K. Ando, K. Takanashi *et al.*, Transmission of electrical signals by spin-wave interconversion in a magnetic insulator, *Nature (London)* **464**, 262 (2010).
- [15] K. Ganzhorn, S. Klingler, T. Wimmer, S. Geprägs, R. Gross, H. Huebl, and S. T. B. Goennenwein, Magnon-based logic in a multi-terminal YIG/Pt nanostructure, *Appl. Phys. Lett.* **109**, 022405 (2016).
- [16] D. Eliyahu and L. Maleki, Tunable, ultra-low phase noise YIG based opto-electronic oscillator, in *Proceedings of the IEEE MTT-S International Microwave Symposium Digest (IEEE, Piscataway, NJ, 2003)*, Vol. 3, pp. 2185–2187.
- [17] A. Qaiumzadeh, H. Skarsvåg, C. Holmqvist, and A. Brataas, Spin Superfluidity in Biaxial Antiferromagnetic Insulators, *Phys. Rev. Lett.* **118**, 137201 (2017).
- [18] R. Khymyn, I. Lisenkov, V. Tiberkevich, B. A. Ivanov, and A. Slavin, Antiferromagnetic THz-frequency Josephson-like oscillator driven by spin current, *Sci. Rep.* **7**, 43705 (2017).
- [19] I. Lisenkov, R. Khymyn, J. Åkerman, N. X. Sun, and B. A. Ivanov, Subterahertz ferrimagnetic spin-transfer torque oscillator, *Phys. Rev. B* **100**, 100409(R) (2019).
- [20] P. Zhang, C.-T. Chou, H. Yun, B. C. McGoldrick, J. T. Hou, K. A. Mkhoyan, and L. Liu, Control of Néel Vector with Spin-Orbit Torques in an Antiferromagnetic Insulator with Tilted Easy Plane, *Phys. Rev. Lett.* **129**, 017203 (2022).
- [21] Y. Takeuchi, Y. Yamane, J.-Y. Yoon, R. Itoh, B. Jinnai, S. Kanai, J. Ieda, S. Fukami, and H. Ohno, Chiral-spin rotation of non-collinear antiferromagnet by spin-orbit torque, *Nat. Mater.* **20**, 1364 (2021).
- [22] R. Wolfe, R. C. LeCraw, S. L. Blank, and R. D. Pierce, (110) bubble garnet films with growth-induced orthorhombic anisotropy, *Appl. Phys. Lett.* **29**, 815 (1976).
- [23] T. Hibiya, H. Makino, and S. Konishi, New bubble garnet films with orthorhombic magnetic anisotropy and high mobility:  $(\text{YBi})_3(\text{FeGa})_5\text{O}_{12}$  and  $(\text{YTmBi})_3(\text{FeGa})_5\text{O}_{12}/(110)\text{GGG}$ , *J. Appl. Phys.* **52**, 7347 (1981).
- [24] A. B. Voermans, D. J. Breed, W. van Erk, and F. M. A. Carpay, Bubble device materials with orthorhombic anisotropy, *J. Appl. Phys.* **50**, 7827 (1979).
- [25] W. T. Stacy, A. B. Voermans, and H. Logmans, Orthorhombic magnetic anisotropy in garnet epitaxial films containing europium, *J. Appl. Phys.* **48**, 4634 (1977).
- [26] W. T. Stacy, A. B. Voermans, and H. Logmans, Increased domain wall velocities due to an orthorhombic anisotropy in garnet epitaxial films, *Appl. Phys. Lett.* **29**, 817 (1976).
- [27] D. J. Breed, P. Q. J. Nederpel, and W. de Geus, Domain-wall dynamics in garnet films with orthorhombic anisotropy, *J. Appl. Phys.* **54**, 6577 (1983).
- [28] H. Callen, Growth-induced anisotropy by preferential site ordering in garnet crystals, *Appl. Phys. Lett.* **18**, 311 (1971).
- [29] D. S. Chuang, C. A. Ballentine, and R. C. O'Handley, Surface and step magnetic anisotropy, *Phys. Rev. B* **49**, 15084 (1994).
- [30] K. M. Krishnan, *Fundamentals and Applications of Magnetic Materials* (Oxford University Press, Oxford, 2016).
- [31] E. Rosenberg, J. Bauer, E. Cho, A. Kumar, J. Pellicciari, C. A. Occhialini, S. Ning, A. Kaczmarek, R. Rosenberg, J. W. Freeland, Y. Chen, J. Wang, J. LeBeau, R. Comin, F. M. F. de Groot, and C. A. Ross, Revealing site occupancy in a complex oxide: Terbium iron garnet, *Small* **19**, 2300824 (2023).
- [32] S. M. Zanjani and M. C. Onbaşlı, Predicting new iron garnet thin films with perpendicular magnetic anisotropy, *J. Magn. Mater.* **499**, 166108 (2020).
- [33] A. H. Eschenfelder, *Magnetic Bubble Technology*, Vol. 14 (Springer, Berlin, 1980).
- [34] T. B. Bateman, Elastic moduli of single-crystal europium iron garnet and yttrium iron garnet, *J. Appl. Phys.* **37**, 2194 (1966).
- [35] E. W. Lee, Physics of Magnetic Garnets Proceedings of the International School of Physics 'Enrico Fermi', *Phys. Bull.* **30**, 533 (1979).
- [36] M. X. Guo, C. K. Cheng, Y. C. Liu, C. N. Wu, W. N. Chen, T. Y. Chen, C. T. Wu, C. H. Hsu, S. Q. Zhou, C. F. Chang, L. H. Tjeng, S. F. Lee, C. F. Pai, M. Hong, and J. Kwo, Single-crystal epitaxial europium iron garnet films with strain-induced perpendicular magnetic anisotropy: Structural, strain, magnetic, and spin transport properties, *Phys. Rev. Mater.* **6**, 054412 (2022).
- [37] H. Nakayama, M. Althammer, Y.-T. Chen, K. Uchida, Y. Kajiwara, D. Kikuchi, T. Ohtani, S. Geprägs, M. Opel, S. Takahashi, R. Gross, G. E. W. Bauer, S. T. B. Goennenwein, and E. Saitoh, Spin Hall Magnetoresistance Induced by a Nonequilibrium Proximity Effect, *Phys. Rev. Lett.* **110**, 206601 (2013).
- [38] Y.-T. Chen, S. Takahashi, H. Nakayama, M. Althammer, S. T. B. Goennenwein, E. Saitoh, and G. E. W. Bauer, Theory of spin Hall magnetoresistance, *Phys. Rev. B* **87**, 144411 (2013).
- [39] C. O. Avci, Current-induced magnetization control in insulating ferrimagnetic garnets, *J. Phys. Soc. Jpn.* **90**, 081007 (2021).
- [40] L. Liu, T. Moriyama, D. C. Ralph, and R. A. Buhrman, Spin-Torque Ferromagnetic Resonance Induced by the Spin Hall Effect, *Phys. Rev. Lett.* **106**, 036601 (2011).
- [41] C. O. Avci, A. Quindeau, C. F. Pai, M. Mann, L. Caretta, A. S. Tang, M. C. Onbasli, C. A. Ross, and G. S. Beach, Current-induced switching in a magnetic insulator, *Nat. Mater.* **16**, 309 (2017).
- [42] R. F. Pearson, Magnetocrystalline anisotropy of rare-earth iron garnets, *J. Appl. Phys.* **33**, 1236 (1962).
- [43] V. H. Ortiz, M. Aldosary, J. Li, Y. Xu, M. I. Lohmann, P. Sellappan, Y. Kadera, J. E. Garay, and J. Shi, Systematic control of strain-induced perpendicular magnetic anisotropy in epitaxial europium and terbium iron garnet thin films, *APL Mater.* **6**, 121113 (2018).
- [44] V. H. Ortiz, B. Arkook, J. Li, M. Aldosary, M. Biggerstaff, W. Yuan, C. Warren, Y. Kadera, J. E. Garay, I. Barsukov, and J. Shi, First- and second-order magnetic anisotropy and damping of europium iron garnet under high strain, *Phys. Rev. Mater.* **5**, 124414 (2021).